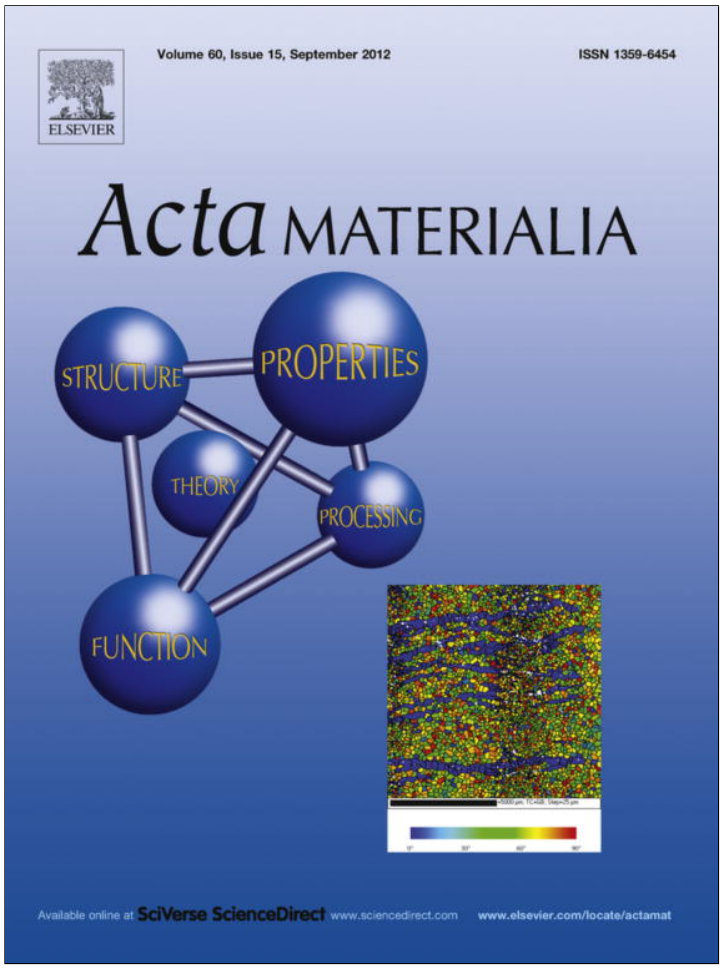

Available online at www.sciencedirect.com

SciVerse ScienceDirect

Acta Materialia 60 (2012) 5578–5592

Acta MATERIALIA

www.elsevier.com/locate/actamat

Phase field approach for simulating solid-state dewetting problems

Wei Jiang [a,b], Weizhu Bao [b,c,*], Carl V. Thompson [d], David J. Srolovitz [e]

[a] Beijing Computational Science Research Center, Beijing 100084, China
[b] Department of Mathematics, National University of Singapore, Singapore 119076, Singapore
[c] Center for Computational Science and Engineering, National University of Singapore, Singapore 119076, Singapore
[d] Department of Materials Science and Engineering, Massachusetts Institute of Technology, Cambridge, MA 02139, USA
[e] Institute of High Performance Computing, 1 Fusionopolis Way, Singapore 138632, Singapore

Received 14 May 2012; received in revised form 1 July 2012; accepted 1 July 2012
Available online 14 August 2012

Abstract

We propose a phase field model for simulating solid-state dewetting and the morphological evolution of patterned islands on a substrate. The evolution is governed by the Cahn–Hilliard equation with isotropic surface tension and variable scalar mobility. The proposed approach easily deals with the complex boundary conditions arising in the solid-state dewetting problem. Since the method does not explicitly track the moving surface, it naturally captures the topological changes that occur during film/island morphology evolution. The numerical method is based on the cosine pseudospectral method together with a highly efficient, stabilized, semi-implicit algorithm. Numerical results on solid-state dewetting in two dimensions demonstrate the excellent performance of the method, including stability, accuracy and numerical efficiency. The method was easily extended to three dimensions (3D), with no essential difference from the two-dimensional algorithm. Numerical experiments in 3D demonstrate the ability of the model to capture many of the complexities that have been observed in the experimental dewetting of thin films on substrates and the evolution of patterned islands on substrates.

Keywords: Solid-state dewetting; Cahn–Hilliard equation; Surface diffusion; Pinch-off phenomena; Cosine pseudospectral method

1. Introduction

In a recent set of experiments on the solid-state dewetting of patterned nickel films on magnesium oxide substrates, Ye and Thompson [1–4] demonstrated the geometric complexity and importance of capillarity-driven instabilities and crystalline anisotropy in dewetting. Solid-state dewetting of thin films plays an important role in microelectronics processing and has also become a common method used to produce nanoparticles (see e.g. [5]) and catalysts for the growth of carbon nanotubes [6] and semiconductor nanowires [7]. In most situations of technological relevance, solid-state dewetting is driven by capillarity effects and occurs through surface diffusion controlled mass transport [8,9]. Although the problem is highly nonlinear, most analytical approaches to modeling solid-state dewetting begin by linearizing the transport equations, treating the problems in reduced dimensions, applying perturbation theory, and/or focusing upon highly simplified geometries [9,10]. The recent experiments by Ye and Thompson [1–4] demonstrate that such approaches miss important phenomena, such as corner-induced instabilities, faceting and the break-up into patterns of islands (pinch-off phenomenon, see Fig. 1). To understand these important phenomena, predict the evolution of complex patterned films and guide new experiments, numerical simulations of the full mathematical problem (including complex geometry, three dimensions (3D) and non-linear equations) represent the most powerful option [11–13].

In general, the dewetting problem belongs to a more general class of capillarity-controlled interface/surface evolution problems. Because the problem includes complex

* Corresponding author at: Department of Mathematics, National University of Singapore, Singapore 119076, Singapore.
E-mail addresses: jiangwei1007@gmail.com (W. Jiang), bao@math.nus.edu.sg (W. Bao), cthomp@mit.edu (C.V. Thompson), srol@ihpc.a-star.edu.sg (D.J. Srolovitz).

1359-6454/$36.00
http://dx.doi.org/10.1016/j.actamat.2012.07.002

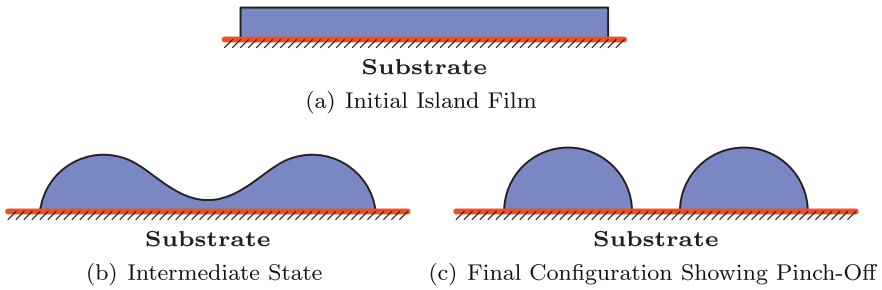

Fig. 1. A two-dimensional schematic illustration of the solid-state dewetting of a thin film on a substrate.

geometry and topology evolution, the phase field approach represents a powerful candidate for simulating this type of problem. The phase field method has been successfully applied to a wide range of problems in materials science, e.g. solidification [14], viscous fingering [15], fracture [16], solid-state nucleation [17] and dislocation dynamics [18]. One of the major advantages of the phase field approach over other explicit interface tracking approaches is its ability to naturally capture the types of topological events that are observed in experiments. It is also straightforward to generalize a simulation from lower to higher spatial dimensions using this approach. The basic idea behind the phase field method is to describe the interface evolution by a partial differential equation for the evolution of an auxiliary field (the phase field) that plays the role of an order parameter. This phase field takes two distinct values (e.g. $+1$ and -1) in each of the two phases bounding an interface and varies smoothly across the interface, i.e. interfaces are diffuse in phase field simulations. In this paper, we develop a phase field approach for modeling and simulating solid-state dewetting. Although we apply this approach to the case of isotropic films on flat substrates, it is easily extended to other interface shapes, and the case of anisotropic surface tension and surface diffusion. For the sake of simplicity, we first develop the method in two dimensions (2D) and then simply extend it to 3D – for the sake of comparison with experiments and because much of the interesting physics only occurs in dimensions larger than two.

The paper is organized as follows. First, we briefly present the sharp interface model for the solid-state dewetting problem, which includes morphology evolution via surface diffusion and contact line migration. We then propose a phase field model for solving the solid-state surface-diffusion-controlled dewetting problem. Next, we present an efficient numerical algorithm, based on a stabilized semi-implicit spectral method, making full use of discrete cosine transforms (DCT) and discrete sine transforms (DST), for solving the governing equations with appropriate boundary conditions. Stability and convergence tests for the new method are then presented for the two- and three-dimensional simulations. Finally, we simulate the evolution of one of the patterned Ni film geometries studied experimentally by Ye and Thompson [2], and show that the agreement is qualitatively excellent.

2. Problem formulation: sharp interface model

The two-dimensional solid-state dewetting of a thin film on a solid substrate can be described in the following form by the Lagrangian representation [11,12]:

$$\frac{d\mathbf{X}}{dt} = V_n \mathbf{n} \tag{2.1}$$

where $\mathbf{X} = (x(s,t), y(s,t))$ represents the evolving solid film/vapor interface (free surface), s is the position along the free surface (i.e. the arclength in 2D), t is time, V_n is the normal velocity of the free surface and $\mathbf{n} = (n_1, n_2)$ is the interface outer unit normal direction (in 2D, $\mathbf{n}$ is a function of s). As a thin solid film evolves via surface diffusion, the normal velocity V_n can be written as described by Mullins [19]:

$$V_n = B\frac{\partial^2 \kappa}{\partial s^2} \tag{2.2}$$

where κ is the mean curvature of the evolving surface (in the two-dimensional case, it is the curvature of the curve), which can be expressed as

$$\kappa = -\frac{\partial^2 y}{\partial s^2}\frac{\partial x}{\partial s} + \frac{\partial^2 x}{\partial s^2}\frac{\partial y}{\partial s} \tag{2.3}$$

and B is a material constant that is proportional to the surface diffusivity and surface (energy) tension.

The governing Eqs. (2.1)–(2.3) for the solid-state dewetting problem are subject to the following boundary conditions:

1. *Contact point condition* (**BC1**)

$$y(x_c, t) = 0 \tag{2.4}$$

where x_c represents the moving contact point where the film, substrate and vapor meet. This point is free to move along the substrate as the surface evolves.

2. *Contact angle condition* (**BC2**)

$$\frac{\partial y/\partial s}{\partial x/\partial s}(x_c, t) = \tan\theta_s \tag{2.5}$$

where $\theta_s \in [0, \pi]$ represents the prescribed contact angle given by the classical Young equation [20], i.e. $\cos\theta_s = (\gamma_{VS} - \gamma_{FS})/\gamma_{FV}$, where γ_{FV}, γ_{FS} and γ_{VS} are, respectively, the interface energy (density) describing the interfaces between film and vapor, film and substrate, and vapor and substrate (see Fig. 2).

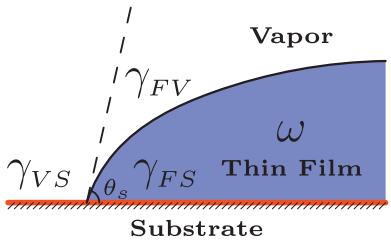

Fig. 2. A schematic illustration of the three interfaces meeting at the contact point. The illustration shows the location (and labels) of the film/vapor (FV), vapor/substrate (VS) and film/substrate (FS) interfaces and the contact angle.

3. *Zero-mass flux condition* (**BC3**)

$$\frac{\partial \kappa}{\partial s}(x_c, t) = 0 \tag{2.6}$$

This condition is necessary for total mass conservation of the film. It implies that there is no mass flux at the contact point – no mass diffuses under the thin film at the film/substrate interface and any flux along the surface to the contact point simply moves the contact point, x_c, such that no flux remains.

Several papers describe earlier approaches to develop numerical algorithms to solve Eqs. (2.1)–(2.3) with the boundary conditions in Eqs. (2.4)–(2.6) [11–13]. These methods are based on front-tracking approaches (or marker particle methods) that employ marker particles to follow the motion of the moving front. Owing to the complex topological changes (such as pinch-off) that occur during dewetting [1–4] and the difficulty of accurately computing fourth-order derivatives along the surface [21,22], these methods must redistribute the marker particles at every time step and, hence, are not easily extendable to 3D or easily describe the topological change events in 3D.

The total interfacial free energy W of the thin film/substrate system can be expressed by

$$W(\omega) = \gamma_{FV}|\Sigma_{FV}| + \underbrace{\gamma_{FS}|\Sigma_{FS}| + \gamma_{VS}|\Sigma_{VS}|}_{\text{Wall Energy}} \tag{2.7}$$

where $|\Sigma_{FV}|$,$|\Sigma_{FS}|$ and $|\Sigma_{VS}|$ represent the corresponding lengths (2D) or areas (3D) of the respective interfaces. The first part of the total free energy in Eq. (2.7) is the total interface energy between the thin film and vapor (we assume that the film/vapor interface energy is isotropic); the other two components refer to the solid substrate and are referred to collectively as the wall energy.

The equilibrium configuration of the system is found by minimizing the total interface free energy subject to conservation of the film volume, i.e. **Min** $W(\omega)$, subject to $\int_\omega \mathrm{d}\omega$ = **Constant**.

3. Phase field model

In order to circumvent the challenging surface tracking within the sharp interface model, we reformulate the problem within a phase field model context that can easily and naturally handle boundary conditions **BC1**–**BC3**, and can be easily extended from 2D to 3D. We start by putting the system into a bounded rectangular box, denoted by Ω with boundary $\partial\Omega = \Gamma_0 \cup \Gamma_1 \cup \Gamma_w$ (see Fig. 3). The phase field function $\phi = \phi(\mathbf{x})$ is introduced such that the zero-level set $\{\mathbf{x}: \phi(\mathbf{x}) = 0\}$ represents the film/vapor interface, while $\{\mathbf{x}: \phi(\mathbf{x}) > 0\}$ represents the film phase and $\{\mathbf{x}: \phi(\mathbf{x}) < 0\}$ the vapor phase.

Corresponding to the total free energy W in Eq. (2.7) in the sharp interface model, the energy functional W^ε can be written, in the phase field framework, as

$$W^\varepsilon = W^\varepsilon_{FV} + W^\varepsilon_w = \int_\Omega f_{FV}\,\mathrm{d}\Omega + \int_{\Gamma_w} f_w\,\mathrm{d}\Gamma_w \tag{3.1}$$

where W^ε_{FV} represents the combined energy of the thin film and vapor phases, W^ε_w represents the wall energy, and f_{FV} and f_w are the corresponding energy densities, respectively. ε is a small parameter that represents the interface width.

The phase field model must satisfy the following conditions in the limit that $\varepsilon \hookrightarrow 0^+$,

- (**C1**) The total free energy W^ε in Eq. (3.1) converges to W in Eq. (2.7). More precisely, the film/vapor phase energy W^ε_{FV} and the wall energy W^ε_w converge to the film/vapor interface energy and wall energy in Eq. (2.7), respectively. At the same time, the minimizers of the functional in Eq. (3.1) also converge to the minimizers of the functional in Eq. (2.7). These requirements are referred to as Γ-convergence [23].
- (**C2**) The "gradient flow" induced by the energy functional in Eq. (3.1) converges to surface diffusion flow with boundary conditions **BC1**–**BC3** within the sharp interface model.

In order to satisfy condition **C1**, we define the film/vapor phase energy density f_{FV} as

$$f_{FV} = \lambda\left(\frac{1}{\varepsilon}F(\phi) + \frac{\varepsilon}{2}|\nabla\phi|^2\right) \tag{3.2}$$

where the first term $F(\phi)$ describes the energy of both the homogeneous film and vapor phases. This can be modeled as the well-known double-well potential, i.e. $F(\phi) = \frac{1}{4}(\phi^2 - 1)^2$. The second term in Eq. (3.2) is the energy density of the interface between the two phases. Finally, the

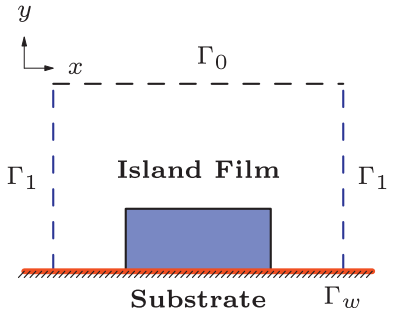

Fig. 3. A schematic illustration of the simulation domain.

parameter λ represents the mixing energy density. The function f_{FV} in Eq. (3.2) is the well-known Ginzburg–Landau free energy density. Modica and Mortola [24] proved that the energy functional W^{ε}_{FV} with energy density f_{FV} defined as Eq. (3.2) Γ-converges to $\gamma_{FV}|\Sigma_{FV}|$ in Eq. (2.7) if the mixing energy density is chosen as

$$\lambda = \frac{3\sqrt{2}}{4}\gamma_{FV} \tag{3.3}$$

The wall energy W^{ε}_{w}, written in terms of the wall energy density f_w, must satisfy: $f_w = \gamma_{VS}$ and $f'_w = 0$ when $\phi = -1$ and $f_w = \gamma_{FS}$ and $f'_w = 0$ when $\phi = 1$. These requirements are satisfied for the wall energy density [25,26]:

$$f_w(\phi) = \frac{\gamma_{VS}+\gamma_{FS}}{2} - \frac{\phi(3-\phi^2)}{4}(\gamma_{VS}-\gamma_{FS}) \tag{3.4}$$

Using this description of the energetics of the system, we now derive the governing dynamical equations for the solid-state dewetting problem within our phase field framework. We first calculate the first variation of energy functional W^{ε} with respect to the phase function ϕ for all smooth functions ψ within our domain ($\forall \psi \in C^{\infty}(\Omega)$),

$$\begin{aligned}\frac{1}{\lambda}\frac{\mathrm{d}}{\mathrm{d}t}W^{\varepsilon}(\phi+t\psi)|_{t=0} &= \int_{\Omega}\left(\frac{1}{\varepsilon}F'(\phi)\psi + \varepsilon\nabla\phi\cdot\nabla\psi\right)\mathrm{d}\mathbf{x} \\ &\quad + \int_{\Gamma_w}\frac{f'_w}{\lambda}\psi\,\mathrm{d}s \\ &= \int_{\Omega}\left(\frac{1}{\varepsilon}F'(\phi) - \varepsilon\Delta\phi\right)\psi\,\mathrm{d}\mathbf{x} \\ &\quad + \int_{\Gamma_w}\left(\varepsilon\frac{\partial\phi}{\partial\mathbf{n}} + \frac{f'_w}{\lambda}\right)\psi\ \mathrm{d}s \\ &\quad + \int_{\partial\Omega\setminus\Gamma_w}\varepsilon\frac{\partial\phi}{\partial\mathbf{n}}\psi\,\mathrm{d}s \\ &= \int_{\Omega}\left(\frac{1}{\varepsilon}F'(\phi) - \varepsilon\Delta\phi\right)\psi\,\mathrm{d}\mathbf{x}\end{aligned} \tag{3.5}$$

where the following natural boundary conditions have been used:

$$\varepsilon\frac{\partial\phi}{\partial\mathbf{n}} + \frac{f'_w}{\lambda} = 0, \quad \text{on} \quad \Gamma_w \tag{3.6}$$

$$\frac{\partial\phi}{\partial\mathbf{n}} = 0, \quad \text{on all other parts of the boundary } (\partial\Omega\setminus\Gamma_w) \tag{3.7}$$

The chemical potential μ is the first variational derivative of W^{ε} with respect to the phase function ϕ:

$$\mu = \frac{1}{\lambda}\frac{\delta W^{\varepsilon}}{\delta\phi} = \frac{1}{\varepsilon}F'(\phi) - \varepsilon\Delta\phi \tag{3.8}$$

Hence, the mass flux $\mathbf{j}$ is

$$\mathbf{j} = -M\nabla\mu \tag{3.9}$$

where M is the diffusional mobility of the film material, which is a non-negative function of ϕ. The evolution equation is then given in terms of Fick's second law,

$$\frac{\partial\phi}{\partial t} + \nabla\cdot\mathbf{j} = 0 \tag{3.10}$$

subject to the constraint that no material flows into or out of the domain through its boundary

$$\frac{\partial\mu}{\partial\mathbf{n}} = 0 \quad \text{on} \quad \partial\Omega \tag{3.11}$$

Although these evolution equations are well defined, we must choose a mobility function M. If the mobility M is chosen to be a constant, the above Eqs. (3.8)–(3.10) reduce to the usual Cahn–Hilliard equation [27]. As indicated in **C2** above, we must choose M such that the flow described by Eqs. (3.8)–(3.10) and the energy functional W^{ε} converges to surface diffusion flow in the limit that ε goes to zero. To achieve this objective, it is natural to choose M such that it is non-zero at the interface and near zero in the film and vapor phases. The choice of a mobility function that yields the correct asymptotics for surface diffusion was discussed in Ref. [28]. In this paper, we choose the mobility to be $M = (1-\phi^2)/\varepsilon$. Using formal asymptotics analysis, Cahn et al. showed that the zero-level set of the solution to the Cahn–Hilliard equation with the above phase field function-dependent mobility converges to an interface evolving via surface diffusion in the limit that ε goes to zero [29,30].

For simplicity, we scale the time t as $\tilde{t} = t/\varepsilon^2$; other similarly scaled physical quantities are denoted by a tilde. In this setting, the governing equations for the solid-state dewetting problem can be written in scaled variables as:

$$\begin{cases}\frac{\partial\phi}{\partial t} = \nabla\cdot(\widetilde{M}\ \nabla\tilde{\mu}) \\ \tilde{\mu} = \phi^3 - \phi - \varepsilon^2\Delta\phi\end{cases} \tag{3.12}$$

subject to the following boundary conditions:

- on Γ_w (the red line in Fig. 3)

$$\varepsilon\frac{\partial\phi}{\partial\mathbf{n}} + \frac{\sqrt{2}}{2}(\phi^2-1)\cos\theta_s = 0 \tag{3.13}$$

$$\frac{\partial\tilde{\mu}}{\partial\mathbf{n}} = 0 \tag{3.14}$$

- on the other boundaries of the domain (i.e. $\Gamma_0\cup\Gamma_1 = \partial\Omega\setminus\Gamma_w$ – the black and blue dashed lines in Fig. 3),

$$\frac{\partial\phi}{\partial\mathbf{n}} = 0 \tag{3.15}$$

$$\frac{\partial\tilde{\mu}}{\partial\mathbf{n}} = 0 \tag{3.16}$$

where $\widetilde{M} = 1-\phi^2$. The boundary condition (3.13) follows from the Young equation: $\gamma_{VS}-\gamma_{FS} = \gamma_{FV}\cos\theta_s$, where θ_s is the contact angle, which comes from the natural boundary condition on the first variation of the total free energy functional of the system and yields the contact angle boundary condition (**BC2**) in the sharp interface limit. Boundary conditions (3.14) and (3.16) imply zero-mass flux (**BC3**) in the sharp interface limit. For brevity, we drop the tilde in the governing Eqs. (3.12)–(3.16) in the remainder of the paper.

4. Numerical algorithm

We now present an efficient and accurate numerical algorithm for the solution of the above Cahn–Hilliard Eq. (3.12) with variable scalar mobility and boundary conditions (Eqs. (3.13)–(3.16)).

We first discuss the discretization in time. We propose a stabilized semi-implicit time stepping method with a constant time step $\Delta t > 0$:

$$\begin{cases} \frac{\phi^{n+1}-\phi^n}{\Delta t} = A\varepsilon^2\Delta^2(\phi^n-\phi^{n+1}) + S\Delta(\phi^{n+1}-\phi^n) + \nabla\cdot(M^n\nabla\mu^n) \\ \mu^n = (\phi^n)^3 - \phi^n - \varepsilon^2\Delta\phi^n \end{cases} \tag{4.1}$$

where $\Delta = \frac{\partial^2}{\partial x^2} + \frac{\partial^2}{\partial y^2}$ denotes the Laplacian operator, ϕ^n and μ^n are, respectively, the approximations of ϕ and μ at the time $t = t_n = n\Delta t$, the parameters A and S are stabilizing coefficients, and $M^n = 1 - (\phi^n)^2$. The idea for adding the stabilizing term $A\varepsilon^2\Delta^2(\phi^n - \phi^{n+1})$ to the Cahn–Hilliard equation with an isotropic mobility was discussed in [31]. However, we found that incorporating an additional stabilizing term $S\Delta(\phi^{n+1} - \phi^n)$ is necessary for the interface evolution problems, especially when ε is small. Similar ideas have been applied to the Allen–Cahn equation [32] and the usual Cahn–Hilliard equation [33]. The choices of the two stabilizing parameters A and S are discussed in the next section. It should be noted that this scheme is first-order accurate with respect to time; a corresponding second-order time stepping approach can be constructed by combining a second-order backward difference method for $\frac{\partial\phi}{\partial t}$ with a second-order Adams–Bashforth method for the explicit discretization of the non-linear term [32,33].

Next, we consider the discretization in space. Let $\Omega = [a,b]\times[c,d]$ be a rectangular domain and denote mesh sizes $\Delta x = \frac{b-a}{K}$ and $\Delta y = \frac{d-c}{J}$, with K and J the mesh grid numbers along the x and y directions, respectively. Because the x-direction boundary conditions are equivalent to the boundary conditions $\frac{\partial\phi}{\partial x} = 0$ and $\frac{\partial^3\phi}{\partial x^3} = 0$, we can apply the standard cosine pseudospectral method in the x-direction and a finite difference method in the y-direction. We perform the following truncated cosine expansion for the phase field function:

$$\phi(x,y,t) = \sum_{k=0}^{K-1}\widehat{\phi_k}(y,t)\cos(v_k(x-a)), \quad a < x < b, \quad c < y < d \tag{4.2}$$

where $v_k = \frac{k\pi}{b-a}$ $(k = 0,1,\ldots,K-1)$ is the kth mode wave number, K is an even positive number and $\widehat{\phi_k}$ is the cosine spectral power for the kth mode along the x-direction. Denote the grid points $x_i = a + (i+0.5)\Delta x$ for $i = 0,1,\ldots, K-1$, $y_j = c + j\Delta y$ for $j = 0,1,\ldots,J$, $\phi^n_{i,j}$ the approximation of $\phi(x_i,y_j,t_n)$, and $(\widehat{\phi_k})^n_j$ the approximation of the kth mode $\widehat{\phi_k}(y_j,t_n)$. Using this description, we can write a discretized counterpart of Eq. (4.2) as

$$\phi^n_{i,j} = \sum_{k=0}^{K-1}(\widehat{\phi_k})^n_j\cos(v_k(x_i-a)), \quad i = 0,1,\ldots,K-1, \quad j = 0,1,\ldots,J \tag{4.3}$$

Inserting Eq. (4.3) into Eq. (4.1) and using the orthogonality of the cosine basis functions and a second-order central finite difference method to discretize the derivatives along the y-direction, we obtain

$$\begin{aligned} &\frac{(\widehat{\phi_k})^{n+1}_j - (\widehat{\phi_k})^n_j}{\Delta t} \\ &= -A\varepsilon^2\frac{(\widehat{\phi_k})^{n+1}_{j+2} - 4(\widehat{\phi_k})^{n+1}_{j+1} + 6(\widehat{\phi_k})^{n+1}_j - 4(\widehat{\phi_k})^{n+1}_{j-1} + (\widehat{\phi_k})^{n+1}_{j-2}}{(\Delta y)^4} \\ &\quad - (A\varepsilon^2v_k^4 + Sv_k^2)(\widehat{\phi_k})^{n+1}_j + (2A\varepsilon^2v_k^2 + S) \\ &\quad \times\frac{(\widehat{\phi_k})^{n+1}_{j+1} - 2(\widehat{\phi_k})^{n+1}_j + (\widehat{\phi_k})^{n+1}_{j-1}}{(\Delta y)^2} + (\widehat{P_k})^n_j + (\widehat{Q_k})^n_j \end{aligned} \tag{4.4}$$

where $(\widehat{P_k})^n_j$ is defined as

$$\begin{aligned} &(\widehat{P_k})^n_j \\ &= A\varepsilon^2\frac{(\widehat{\phi_k})^n_{j+2} - 4(\widehat{\phi_k})^n_{j+1} + 6(\widehat{\phi_k})^n_j - 4(\widehat{\phi_k})^n_{j-1} + (\widehat{\phi_k})^n_{j-2}}{(\Delta y)^4} \\ &\quad + (A\varepsilon^2v_k^4 + Sv_k^2)(\widehat{\phi_k})^n_j - (2A\varepsilon^2v_k^2 + S) \\ &\quad \times\frac{(\widehat{\phi_k})^n_{j+1} - 2(\widehat{\phi_k})^n_j + (\widehat{\phi_k})^n_{j-1}}{(\Delta y)^2} \end{aligned} \tag{4.5}$$

and $Q^n = \nabla\cdot(M^n\nabla\mu^n)$, which can be discretized as

$$Q^n_{i,j} = \sum_{k=0}^{K-1}(\widehat{Q_k})^n_j\cos(v_k(x_i-a)), \quad i = 0,1,\ldots,K-1, \quad j = 0,1,\ldots,J \tag{4.6}$$

We discuss below how to compute the kth mode spectral power $(\widehat{Q_k})^n_j$. For simplicity, Eq. (4.4) can be written in the following nearly diagonal (i.e. penta-diagonal) matrix form:

$$\begin{aligned} &a_{-2}(\widehat{\phi_k})^{n+1}_{j-2} + a_{-1}(\widehat{\phi_k})^{n+1}_{j-1} + a_0(\widehat{\phi_k})^{n+1}_j + a_1(\widehat{\phi_k})^{n+1}_{j+1} \\ &+ a_2(\widehat{\phi_k})^{n+1}_{j+2} = R^n_j, \quad j = 0,1,\ldots,J \end{aligned} \tag{4.7}$$

where the terms on the right-hand side R^n_j are

$$R^n_j = (\widehat{\phi_k})^n_j + ((\widehat{P_k})^n_j + (\widehat{Q_k})^n_j)\Delta t \tag{4.8}$$

and the coefficients a_l for $l = -2,-1,0,1,2$ are given as

$$a_{-2} = a_2 = A\varepsilon^2\frac{\Delta t}{(\Delta y)^4} \tag{4.9}$$

$$a_{-1} = a_1 = -4A\varepsilon^2\frac{\Delta t}{(\Delta y)^4} - (2A\varepsilon^2v_k^2 + S)\frac{\Delta t}{(\Delta y)^2} \tag{4.10}$$

$$a_0 = 1 + (A\varepsilon^2v_k^4 + Sv_k^2)\Delta t + 6A\varepsilon^2\frac{\Delta t}{(\Delta y)^4} + (4A\varepsilon^2v_k^2 + 2S)\frac{\Delta t}{(\Delta y)^2} \tag{4.11}$$

In order to solve the matrix algebra Eq. (4.7), we consider the boundary conditions along the y-direction (shown by Γ_0 and Γ_w in Fig. 3). On the boundary Γ_0, the boundary conditions (3.15) and (3.16) can be expressed as $\frac{\partial \widehat{\phi_k}}{\partial y} = 0$ and $\frac{\partial^3 \widehat{\phi_k}}{\partial y^3} = 0$. By using the central difference method, the values of the ghost points $(\widehat{\phi_k})_{J+1}^{n+1}$ and $(\widehat{\phi_k})_{J+2}^{n+1}$ involved in Eq. (4.7) can be obtained as: $(\widehat{\phi_k})_{J+1}^{n+1} = (\widehat{\phi_k})_{J-1}^{n+1}$ and $(\widehat{\phi_k})_{J+2}^{n+1} = (\widehat{\phi_k})_{J-2}^{n+1}$. Similarly, we can express boundary conditions (3.13) and (3.14) on Γ_w by

$$\varepsilon \frac{\partial \widehat{\phi_k}}{\partial y} = \frac{\sqrt{2}}{2} \cos\theta_s \widehat{B_k}, \qquad \frac{\partial^3 \widehat{\phi_k}}{\partial y^3} = 0 \qquad \text{on} \quad \Gamma_w \tag{4.12}$$

where $\widehat{B_k}$ is defined as the kth mode cosine spectral power of the function $\phi^2 - 1$ defined on Γ_w, i.e. $(\phi^2 - 1)|_{y=c} = \sum_{k=0}^{K-1} \widehat{B_k}(t)\cos(v_k(x-a))$, $a < x < b$. Following the above definition and using the central difference method, we can obtain the discretized boundary conditions on Γ_w as $(\widehat{\phi_k})_{-1}^{n+1} = (\widehat{\phi_k})_{1}^{n+1} - \frac{\sqrt{2}}{\varepsilon}\cos\theta_s (\widehat{B_k})^n \Delta y$ and $(\widehat{\phi_k})_{-2}^{n+1} = (\widehat{\phi_k})_{2}^{n+1} - \frac{2\sqrt{2}}{\varepsilon}\cos\theta_s (\widehat{B_k})^n \Delta y$. Inserting these values for the ghost points into Eq. (4.7), we obtain $J+1$ unknown variables and $J+1$ algebraic equations. Fast algorithms for solving a penta-diagonal matrix system are available [34] and can be easily applied to solve these equations.

We now address the question of how to compute the kth mode spectral power $(\widehat{Q_k})_j^n$ of the non-linear term Q^n. This term can be divided into two parts, i.e. $Q^n = \frac{\partial}{\partial x}\left(M^n \frac{\partial \mu^n}{\partial x}\right) + \frac{\partial}{\partial y}\left(M^n \frac{\partial \mu^n}{\partial y}\right)$. The first two terms of $\mu^n = (\phi^n)^3 - \phi^n - \varepsilon^2 \Delta \phi^n$ may be denoted as $g^n = (\phi^n)^3 - \phi^n$ and expressed as a truncated cosine expansion: $g_{i,j}^n = \sum_{k=0}^{K-1} (\widehat{g_k})_j^n \cos(v_k(x_i - a))$, $i = 0, 1, \ldots, K-1$, $j = 0, 1, \ldots, J$. Making use of Eq. (4.3) and the central finite difference method to discretize the derivatives along the y-direction, we obtain

$$\left(\frac{\partial \mu^n}{\partial x}\right)_{i,j}^n = \sum_{k=1}^{K-1} (\widehat{\mu_k^x})_j^n \sin(v_k(x_i - a)), \quad i = 0, 1, \ldots, K-1, \quad j = 0, 1, \ldots, J \tag{4.13}$$

$$\left(\frac{\partial \mu^n}{\partial y}\right)_{i,j}^n = \sum_{k=1}^{K-1} (\widehat{\mu_k^y})_j^n \cos(v_k(x_i - a)), \quad i = 0, 1, \ldots, K-1, \quad j = 0, 1, \ldots, J \tag{4.14}$$

where the kth mode spectral power $(\widehat{\mu_k^x})_j^n$ and $(\widehat{\mu_k^y})_j^n$ are defined as

$$(\widehat{\mu_k^x})_j^n = -v_k (g_k)_j^n - \varepsilon^2 \left(v_k^3 (\widehat{\phi_k})_j^n - v_k \frac{(\widehat{\phi_k})_{j+1}^n + (\widehat{\phi_k})_{j-1}^n - 2(\widehat{\phi_k})_j^n}{(\Delta y)^2} \right) \tag{4.15}$$

$$(\widehat{\mu_k^y})_j^n = \frac{(g_k)_{j+1}^n - (g_k)_{j-1}^n}{2\Delta y} + \varepsilon^2 \left(v_k^2 \frac{(\widehat{\phi_k})_{j+1}^n - (\widehat{\phi_k})_{j-1}^n}{2\Delta y} - \frac{(\widehat{\phi_k})_{j+2}^n - 2(\widehat{\phi_k})_{j+1}^n + 2(\widehat{\phi_k})_{j-1}^n - (\widehat{\phi_k})_{j-2}^n}{2(\Delta y)^3} \right) \tag{4.16}$$

Then we obtain $\left(\frac{\partial \mu^n}{\partial x}\right)_{i,j}^n$ and $\left(\frac{\partial \mu^n}{\partial y}\right)_{i,j}^n$ by performing an inverse discrete sine/cosine transform. We can compute the kth mode values of $(\widehat{Q_k})_j^n$ following a similar procedure. It should be noted that our algorithm requires the computation of a large number of DCT and DST. These can be easily accomplished using the well-known numerical computational software FFTW package [35]. Finally, the steps of our proposed numerical algorithm are summarized as follows:

- **Step 1**: Given the phase function ϕ^n at the time $t = t_n$.
- **Step 2**: Compute the kth mode spectral power $(\widehat{\phi_k})_j^n$ by using DCT along the x-direction.
- **Step 3**: Compute the kth mode spectral power $(\widehat{P_k})_j^n$ by using Eq. (4.5).
- **Step 4**: Use the DCT and DST to compute the kth mode spectral power $(\widehat{Q_k})_j^n$ of the non-linear term.
- **Step 5**: Compute the coefficients a_l, $(\widehat{B_k})^n$, R_j^n and solve the linear system (4.7) to obtain $(\widehat{\phi_k})_j^{n+1}$.
- **Step 6**: Perform an inverse discrete cosine transform to $(\widehat{\phi_k})_j^{n+1}$ to obtain the phase function ϕ^{n+1} at the time $t = t_{n+1}$.
- **Step 7**: Repeat **Step 3** through **Step 6** until the prescribed stop criterion is satisfied.

5. Results and discussion

In this section, we present several simulation results using the phase field method proposed above to determine appropriate stabilizing constants to demonstrate its accuracy, and show example applications in two and three spatial dimensions. The simulations were performed within simulation cells which were uniformly meshed, discretized with 512×256 grid points in 2D and $256 \times 256 \times 128$ grid points in 3D except where noted.

5.1. Stability test

There are two important parameters, A and S, that are related to the stabilizing terms in the numerical algorithm proposed above. By performing a series of numerical experiments, we determined that $A = 0.5$ and $S = 1.0$ allows an excellent compromise between numerical stability, accuracy and computational efficiency. Table 1 shows that adding the stabilizing term $S\Delta(\phi^{n+1} - \phi^n)$ in our numerical scheme (4.1) greatly increases the size of the maximum allowable time steps. We define the maximum allowable time step $\Delta t_{\max}$ as the largest time step for which our numerical scheme is stable. Table 1 shows that adding a non-zero stabilizing parameter S can increase the size of $\Delta t_{\max}$ by several orders of magnitude; the increase is more pronounced with decreasing ε.

While the inclusion of stabilizing terms greatly increases the maximum time step for which the algorithm is stable, these terms will inevitably produce some level of consistency

Table 1
Allowed maximum time step $\Delta t_{\max}$ with different A and S.

ε	A,S	$\Delta t_{\max}$
$\varepsilon = 0.01$	$A = 0.0$, $S = 0.0$	$\Delta t_{\max} < 1.0 \times 10^{-7}$
	$A = 0.5$, $S = 0.0$	$\Delta t_{\max} \approx 2.0 \times 10^{-3}$
	$A = 0.5$, $S = 1.0$	$\Delta t_{\max} \approx 9.0 \times 10^{-1}$
$\varepsilon = 0.001$	$A = 0.0$, $S = 0.0$	$\Delta t_{\max} < 1.0 \times 10^{-7}$
	$A = 0.5$, $S = 0.0$	$\Delta t_{\max} \approx 1.0 \times 10^{-5}$
	$A = 0.5$, $S = 1.0$	$\Delta t_{\max} \approx 3.0 \times 10^{-1}$

error. This consistency error is of the same order as the error produced by the explicit treatment of the non-linear term and can be diminished by reducing the time step size. In real applications, a compromise must be struck between these two competing considerations. Fig. 4 shows a comparison of the numerical results produced by using three different sets of stabilizing parameters and time steps over a range of times from near the initial condition to near the equilibrium state ($t = 1$,10, 50 and 200). From the numerical results (see Fig. 4), we observe that, in comparison with choosing a zero stabilizing parameter S and a very small time step size $\Delta t = 0.0001$, our choices of $S = 1.0$ and $\Delta t = 0.01$ produce numerical results that accurately capture the evolution dynamics with a time step that is many orders of magnitude larger than that without the inclusion of stabilizing terms. This demonstrates that our method is suitable for long-time simulations.

5.2. Convergence test

We next address the issue of convergence of the proposed method by performing simulations in which the initial state of the thin film island is a rectangle, located in $[-0.5, 0.5] \times [0, 0.2]$ of a $[-1, 1] \times [0, 1]$ computational domain Ω. The mesh size is denoted as $h = \Delta x = \Delta y$ and the time step is fixed as $\Delta t = 0.5h$. Because the size of the initial rectangle is small relative to that of the computational domain, the Young angle is positive, mass (film area) is conserved and the surface energy density is isotropic, the equilibrium shape of the thin film island will be a predictable truncated circle. In the following discussion, we examine how the evolving shape converges to the theoretical equilibrium state.

Since the initial island shape does not satisfy the Young contact angle boundary condition, it is instructive to see how quickly that angle is established and maintained by the numerical algorithm. We first define the numerical contact angle θ_n at step n in the evolution using the procedure suggested in Fig. 5. Suppose that A, B and C are three points on the film/vapor interface as represented by the zero-level set $\{\mathbf{x}: \phi(\mathbf{x}) = 0\}$. Point A is the left contact point between the interface and the substrate with coordinates $(P_n, 0)$. Points B and C are, respectively, the intersection points between the interface and the meshline $y = h$ or $y = 2h$ with coordinates (x_1, h) and $(x_2, 2h)$. To determine the numerical wetting angle, we fit a circle to these three points and determine the angle from the tangent line of the fitted circle at the contact point A. A similar definition for the numerical contact angle was used in Ref. [36].

The numerical simulations were terminated when the island shape achieves the equilibrium state, defined numerically as the time at which $\|\phi^{n+1} - \phi^n\|_{l_2} < 10^{-6}$ is first satisfied, where $\|\cdot\|_{l_2}$ represents the discrete l_2 norm. Fig. 6 and Table 2 show the convergence results of the numerical equilibrium state compared with the theoretical equilibrium state by reducing the parameter ε for two different

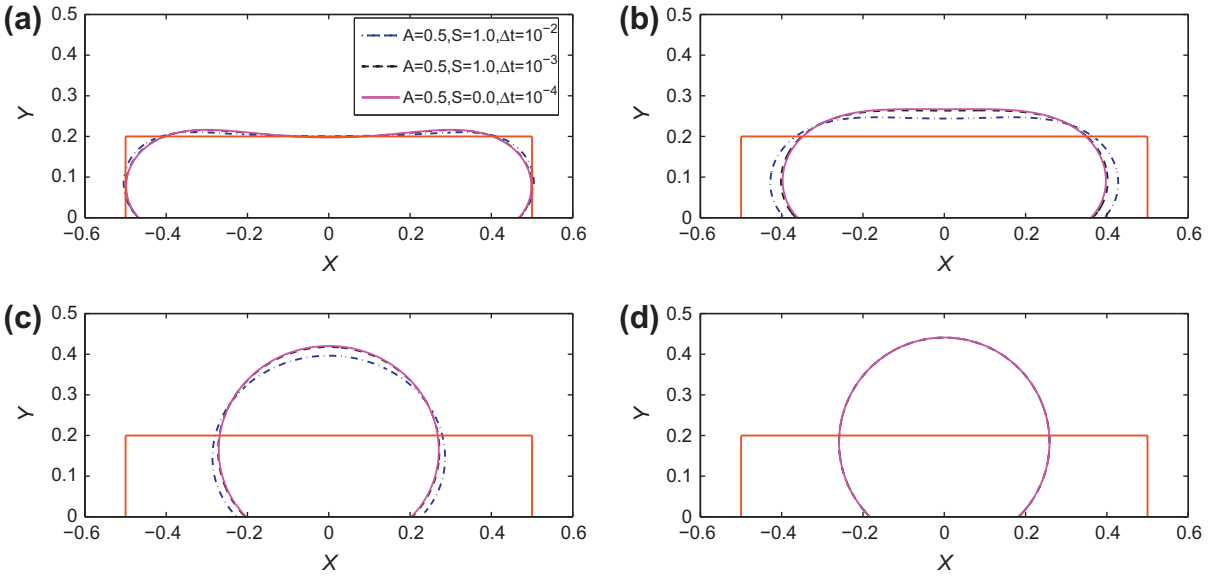

Fig. 4. Two-dimensional numerical results produced using different stabilizing parameters and time steps for the same parameters, $\varepsilon = 0.01$, $\theta_s = 3\pi/4$, at four different times: (a) $t = 1$, (b) $t = 10$, (c) $t = 50$ and (d) $t = 200$. The initial condition was a rectangular island film located in the region $[-0.5, 0.5] \times [0, 0.2]$ (labeled as red lines). (For interpretation of the references to colour in this figure legend, the reader is referred to the web version of this article.)

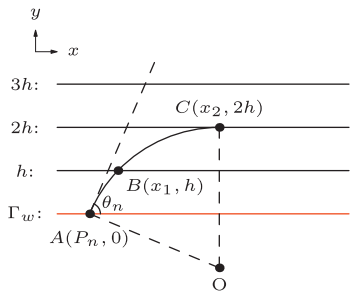

Fig. 5. A schematic illustration of the procedure used to determine the numerical contact angle.

Table 2
Convergence results to the contact angle and contact point position of theoretical equilibrium state obtained by reducing ε.

ε	$\varepsilon = 0.04$	$\varepsilon = 0.02$	$\varepsilon = 0.01$	$\varepsilon = 0.005$	θ_s
θ_n	2.263	2.313	2.336	2.349	$\frac{3\pi}{4} \approx 2.356$
(rad)	0.7306	0.7629	0.7708	0.7748	$\pi/4 \approx 0.7854$
$\alpha_{\mathbf{err}}$	−0.03974	−0.01850	−0.008528	−0.003083	
	−0.06979	−0.02870	−0.01857	−0.01048	
ε	$\varepsilon = 0.04$	$\varepsilon = 0.02$	$\varepsilon = 0.01$	$\varepsilon = 0.005$	x_c
P_n	−0.1693	−0.1792	−0.1831	−0.1851	−0.1871 $\theta_s = \frac{3\pi}{4}$
	−0.5732	−0.5852	−0.5902	−0.5925	−0.5919 $\theta_s = \pi/4$
$\beta_{\mathbf{err}}$	−0.09514	−0.04222	−0.02138	−0.01069	
	−0.03159	−0.01132	−0.002872	0.001014	

contact angles, $\theta_s = 3\pi/4$ and $\theta_s = \pi/4$. The computational parameters are set to $\varepsilon = 0.04/n$ and $h = 1/(64n)$, for $n = 1, 2, 4, 8$. Fig. 6 clearly shows that the numerical equilibrium states (see the black lines) converge to the theoretical equilibrium state (shown by the blue lines) on reducing ε. Table 2 shows the convergence of the contact angle θ_n and the (left) numerical contact point position P_n at the numerical equilibrium state to their theoretical equilibrium counterparts. We define the relative error of the contact angle as $\alpha_{\mathbf{err}} = (\theta_n - \theta_s)/\theta_s$ and the relative error of the left contact point position as $\beta_{\mathbf{err}} = (P_n - x_c)/x_c$, where x_c represents the theoretical equilibrium contact point position. Table 2 shows that the relative errors $\alpha_{\mathbf{err}}$ and $\beta_{\mathbf{err}}$ both converge to zero with approximately first-order accuracy with decreasing ε.

5.3. Two-dimensional simulations

In this section, we report several two-dimensional applications of the wetting/dewetting phase field simulation method presented above. First, we examine the evolution of an island on the substrate under different prescribed contact angles.The thin film island is initially occupied in the region $[-0.5, 0.5] \times [0, 0.2]$; the computational parameters were employed as: $\Omega = [-1, 1] \times [0, 1]$, $\varepsilon = 0.01$, $\Delta t = 0.1h$ and $h = 1/256$. Fig. 7 shows the relative error $\alpha_{\mathbf{err}}$ in the contact angle as a function of time, normalized by t_s (defined above as the time at which the numerical equilibrium state is first achieved). The figure shows that the relative error $\alpha_{\mathbf{err}}$ decays exponentially to a very low ($\leqslant 5\%$) level (in a time $\sim 10^{-6} t_s$) under all prescribed contact angles. This demonstrates that the simulation is capable of achieving numerical contact angles θ_n in excellent agreement with the prescribed contact angle θ_s over all meaningful times during the evolution.

The evolution of the island towards its equilibrium morphology is shown in Fig. 8 for several prescribed contact

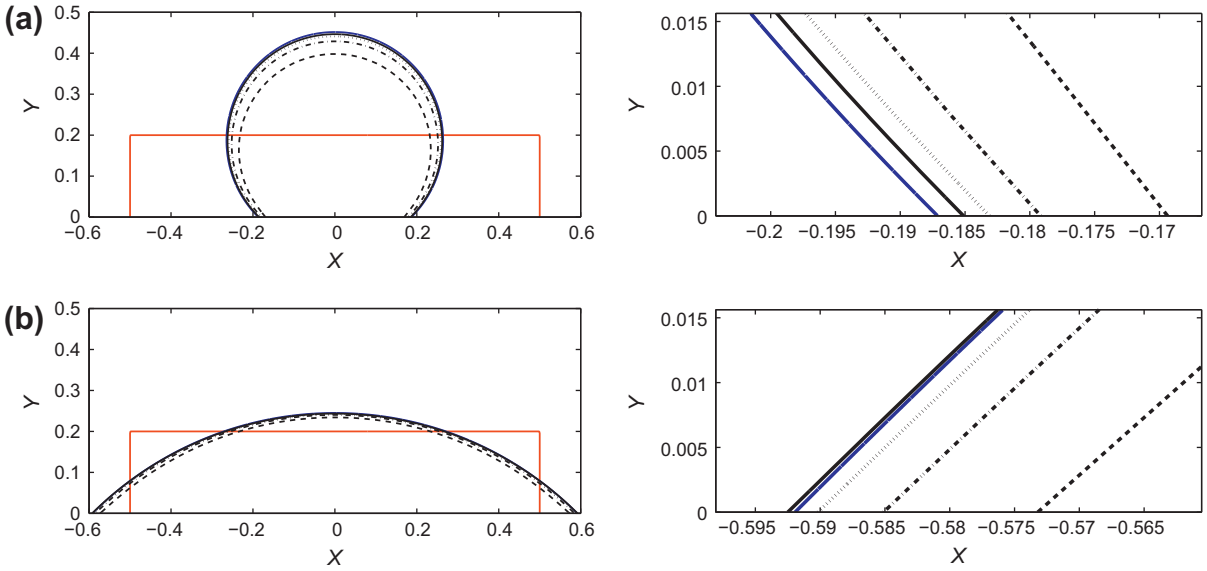

Fig. 6. Convergence results to the theoretical equilibrium state (label as **blue** lines) obtained by using different ε under the prescribed contact angles: (a) $\theta_s = 3\pi/4$ and (b) $\theta_s = \pi/4$. The figures in the right column are enlargements of those in the left column near the left contact point. The black lines show the numerical equilibrium states under different ε, i.e. dashed lines ($\varepsilon = 0.04$), dash-dotted lines ($\varepsilon = 0.02$), dotted lines ($\varepsilon = 0.01$) and solid lines ($\varepsilon = 0.005$). The initial state of the film is shown as red lines. (For interpretation of the references to colour in this figure legend, the reader is referred to the web version of this article.)

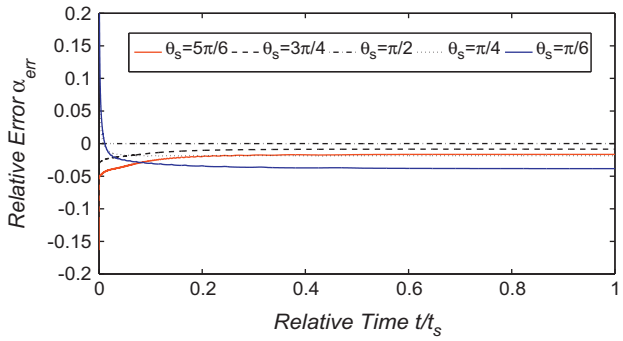

Fig. 7. Relative error between the numerical contact angle θ_n and the prescribed contact angle θ_s as a function of time normalized by t_s.

angle $0 \leqslant \theta_s \leqslant \pi$. From these figures, we clearly see that the prescribed contact angle θ_s is rapidly achieved on the timescale that the island evolves towards its equilibrium case. Further, this angle is maintained throughout the island morphology evolution. This includes the extreme cases of complete dewetting $\theta_s = \pi$ (the equilibrium is a full circle that touches the substrate at a point), complete wetting $\theta_s = 0$ (the equilibrium is a continuous film) or any intermediate θ_s. Note that, for the larger values of θ_s, the curvature of the center of the island changes sign during the evolution; this feature occurs when capillarity-driven surface diffusion control the evolution and is absent for many other types of kinetics (e.g. evaporation–condensation) [8,9]. The mass loss during the entire duration of all of the simulations is strictly below 0.1%.

Fig. 9 shows the evolution of a thin film containing a small hole (that extends through the film to the substrate) at its center for $\theta_s = 5\pi/6$ and $\theta_s = \pi/6$. (Note that the finite island and finite hole are actually equivalent because of the use of periodic boundary conditions here – the only qualitative different is the separation of the two island/hole edges relative to the lateral domain size.) The initial film occupies $x \leqslant -0.05$ and $x \geqslant 0.05$, and has a thickness of 0.1. For the $\theta_s = 5\pi/6$ case (see Fig. 9a), the hole grows and eventually achieves the equilibrium circular shape (because of the periodic boundary conditions). However, for $\theta_s = \pi/6$ (see Fig. 9b), the initial hole closes, the valley where the hole was located disappears and the film approaches a metastable flat morphology. The numerical results are consistent with the analysis in Ref. [9].

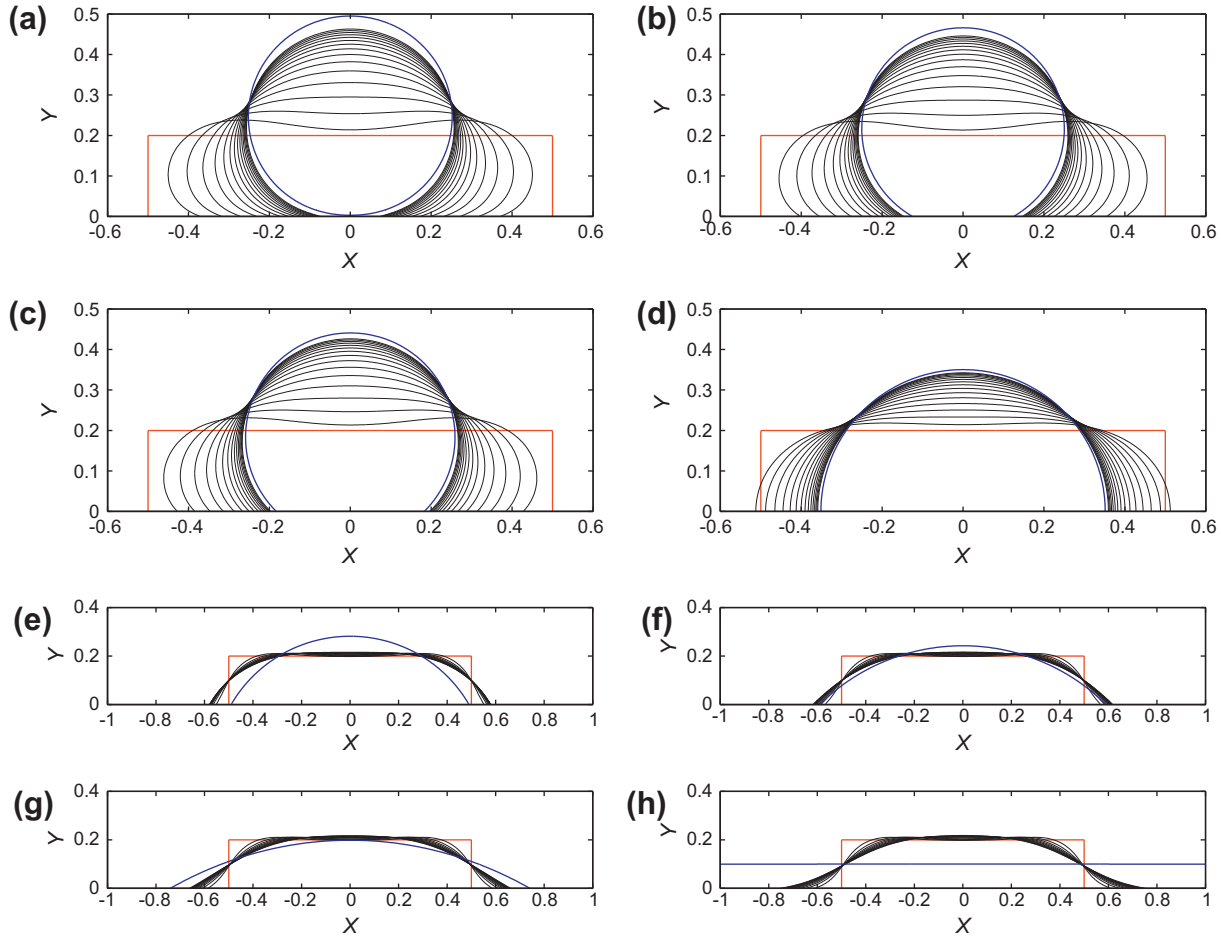

Fig. 8. Several steps of the evolution of initially rectangular islands (shown in red) toward their equilibrium shapes (shown in blue) for eight different prescribed contact angles: (a) $\theta_s = \pi$, (b) $\theta_s = 5\pi/6$, (c) $\theta_s = 3\pi/4$, (d) $\theta_s = \pi/2$), (e) $\theta_s = \pi/3$, (f) $\theta_s = \pi/4$, (g) $\theta_s = \pi/6$ and (h) $\theta_s = 0$. Images are shown every 10^4 time steps for (a)–(d) or every 10^3 time steps for (e)–(h) (labeled as black lines). (For interpretation of the references to colour in this figure legend, the reader is referred to the web version of this article.)

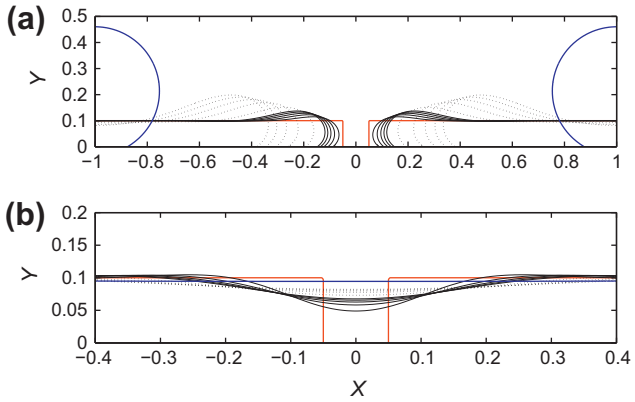

Fig. 9. The evolution of a thin film containing a hole in its center for contact angles: (a) $\theta_s = 5\pi/6$ and (b) $\theta_s = \pi/6$. The film profiles are shown every 500 time steps (solid black lines) and every 5000 time steps (dotted black lines). The red and blue represent the initial and numerical equilibrium states, respectively. (For interpretation of the references to colour in this figure legend, the reader is referred to the web version of this article.)

Next, we consider the evolution of an initially flat, semi-infinite, uniform film (of thickness 0.05) on a substrate. While a simple scaling analysis suggests that the contact point should evolve as t^{β} with $\beta = 1/4$ [9], more recent simulations and analysis suggest that it should evolve with $\beta = 2/5$ [11]. The numerical simulations show that the film contracts via the motion of the contact point and eventually pinches off an island. Fig. 10 shows the evolution of the position of the contact point as the semi-infinite film retracts for several different contact angles (prior to pinch-off). For each contact angle, the contact point

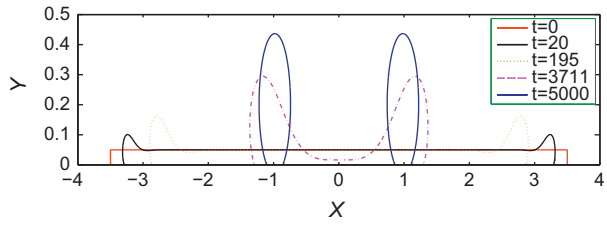

Fig. 11. The evolution of a very long, thin island for a prescribed contact angle $\theta_s = 5\pi/6$. Note that the vertical and horizontal scales in this figure differ significantly.

position as a function of time can be reasonably described by a power law of the form $x_c \propto t^{\beta}$. The fitting suggests that the exponent β decreases with increasing contact angle from 0.53 at $\theta_s = \pi/4$ to 0.41 at $\theta_s = 5\pi/6$ (see Fig. 10). These exponents are significantly larger than $\beta = 1/4$ predicted from the simple scaling analysis [9] and are much closer to the more recent theoretical value of $\beta = 2/5$ [11]. We note that the quality of the power-law fit to the simulation data is better for larger contact angle; this may be related to the relaxation of the initial condition as the retracting film acquires the correct contact angle, the coarse, uniform discretization of the profile near the contact point and the slower evolution of the film profile at a smaller contact angle. Recent experiments on the retraction of contact lines in Ni on MgO show retraction exponents in the $0.40 \leqslant \beta \leqslant 0.60$ range, with values close to 0.4 being the most common [3].

Finally, we performed a series of two-dimensional numerical simulations of the evolution of a very long, thin island. Initially, the island is located in the region

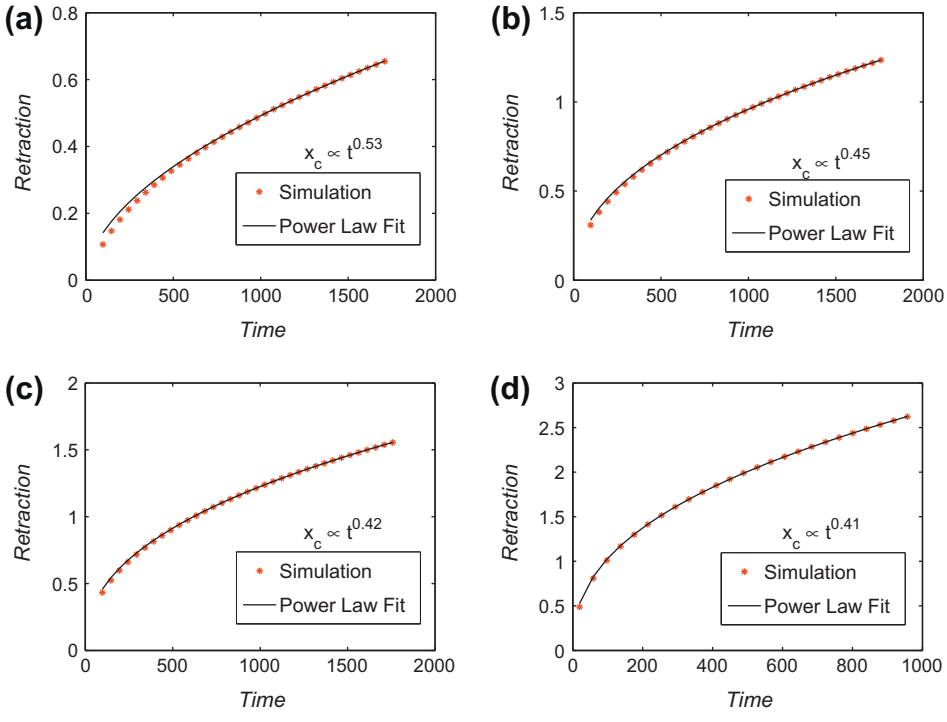

Fig. 10. The power law for the contact point retraction position as a function of time by numerical simulations under different contact angles: (a) $\theta_s = \pi/4$; (b) $\theta_s = \pi/2$; (c) $\theta_s = 3\pi/4$; and (d) $\theta_s = 5\pi/6$.

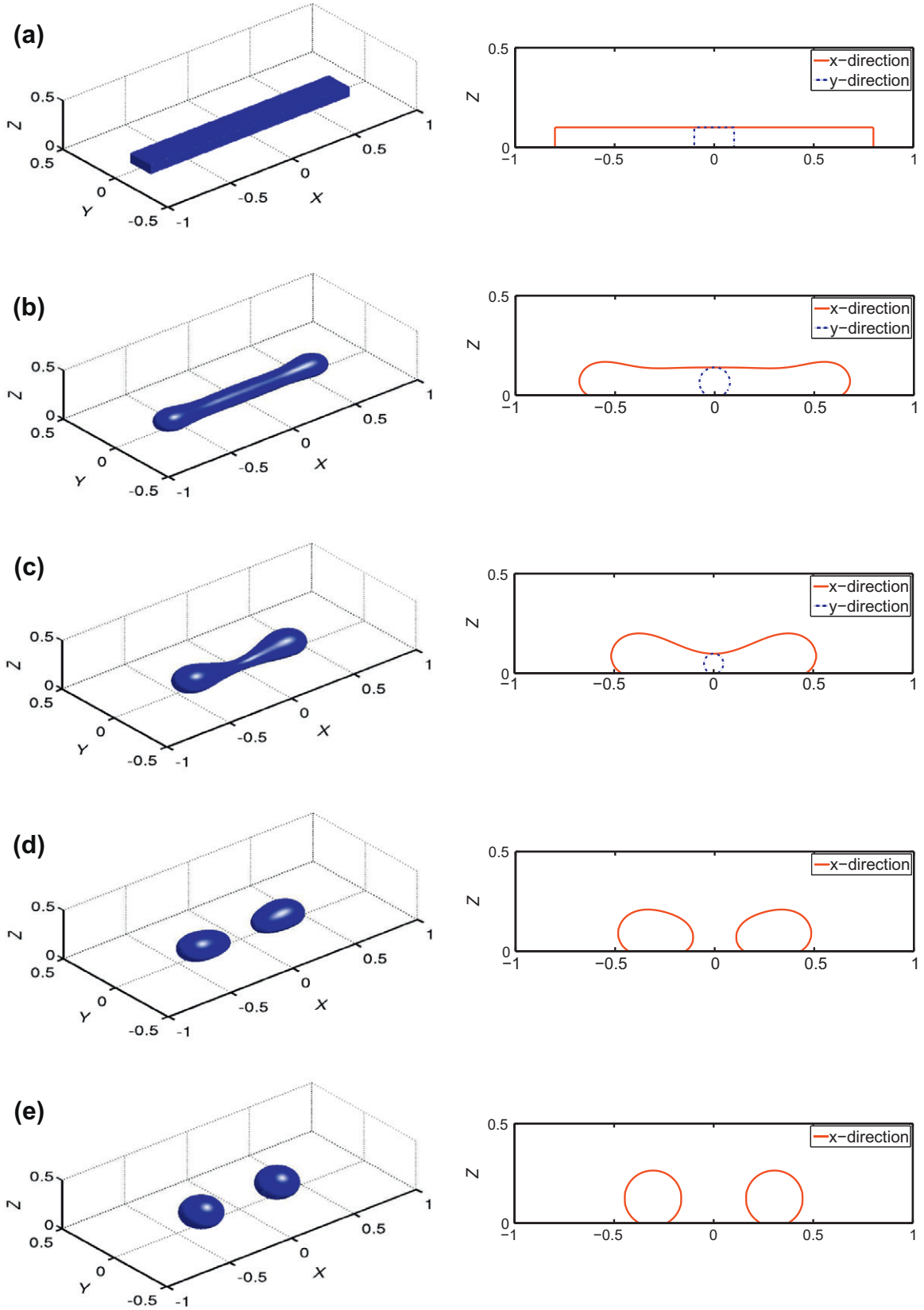

Fig. 12. The evolution of an initially rectangular, thin film island at five times: (a) $t = 0$; (b) $t = 3.91$; (c) $t = 12.50$; (d) $t = 14.84$; and (e) $t = 78.13$. The right column figures show the cross-section profile of the thin film along the x- or y-direction across the origin. The wetting angle is $\theta_s = 5\pi/6$.

$[-3.5, 3.5] \times [0, 0.05]$ (i.e. an aspect ratio of 140), and the computational parameters are $\Omega = [-4.0, 4.0] \times [0, 0.5]$, $\varepsilon = 0.005$, $h = 1/512$, $\Delta t = h$ and the prescribed contact angle $\theta_s = 5\pi/6$. The results are shown in Fig. 11.

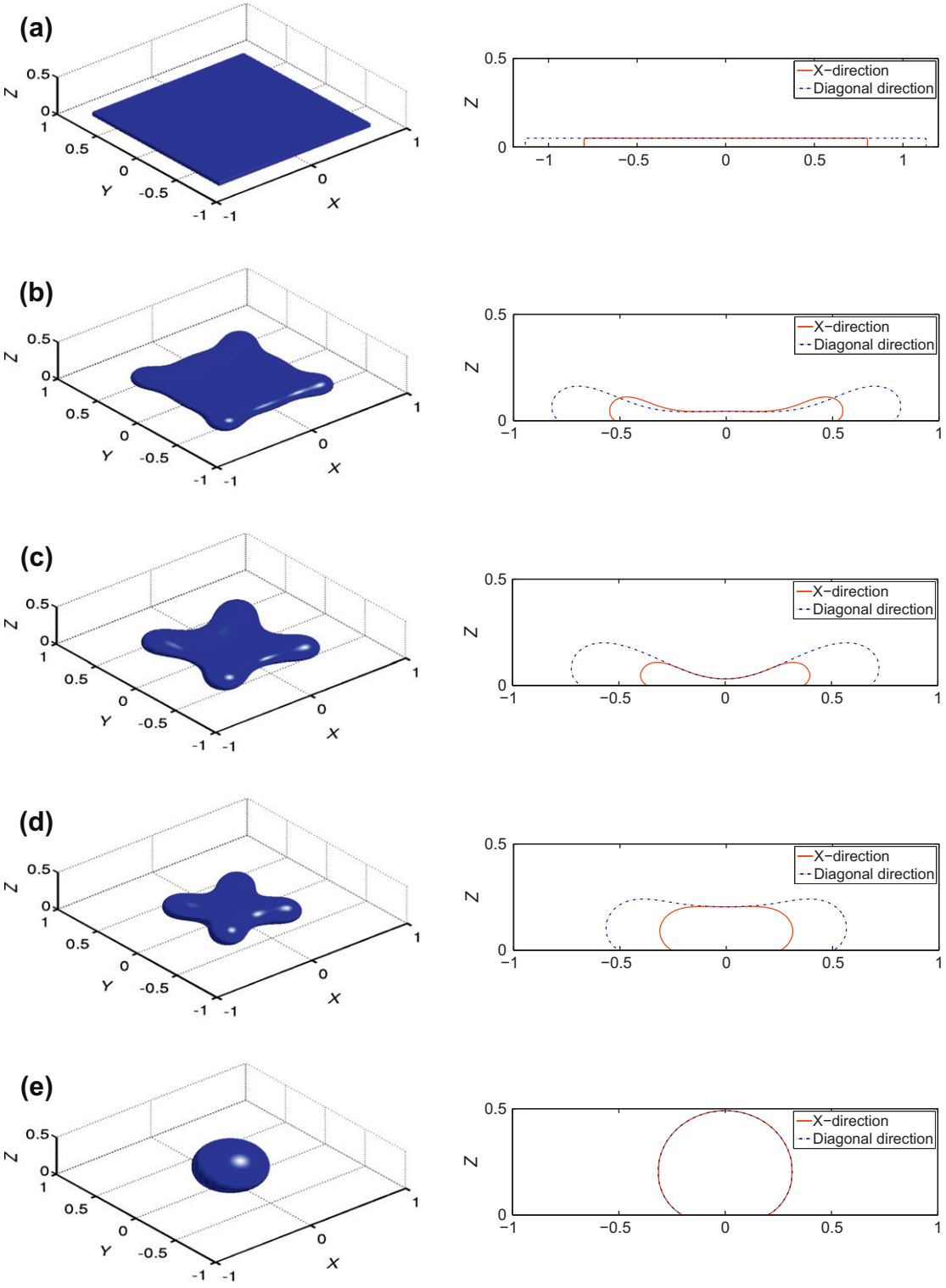

Fig. 13. The temporal evolution of an initially square, small, thin film island at five times for $\theta_s = 5\pi/6$: (a) $t = 0$; (b) $t = 7.81$; (c) $t = 15.63$; (d) $t = 39.06$; and (e) $t = 156.25$. The right column figures show the cross-section profile of the island along the x- or diagonal direction across the origin.

Interestingly, in this case (as in Fig. 8 for large θ_s), the surface diffusion kinetics lead to the formation of a ridge at the edge of the island and minima in the profiles on the sides of the ridge. Both of these features become increasingly exaggerated as the island edge retracts and the two minima merge near the island center. Eventually (between the last two times shown in Fig. 11), the minimum at the center of the islands hits the substrate and two new contact points are formed, breaking the island film into two separate islands, which individually equilibrate. We note

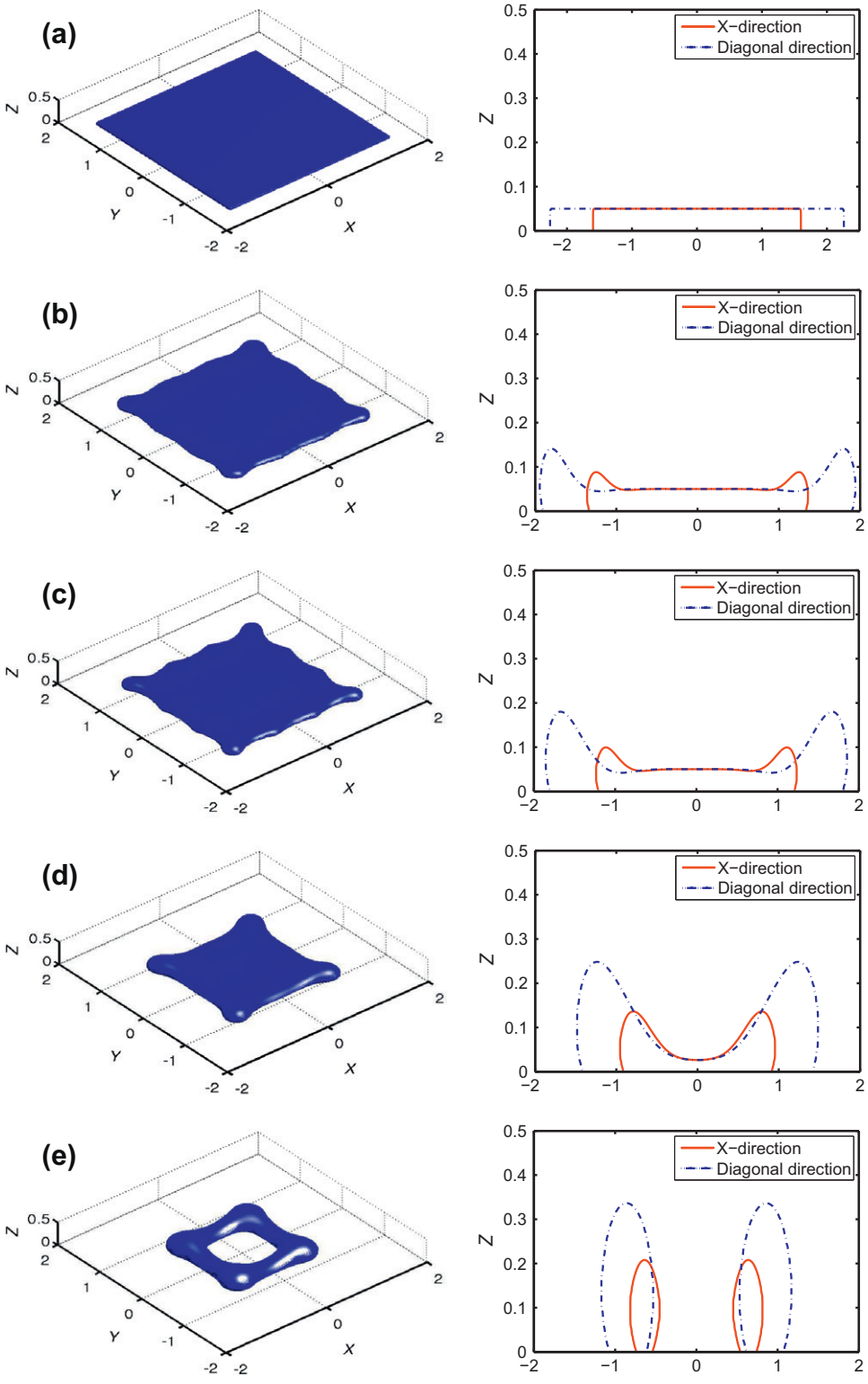

Fig. 14. The temporal evolution of an initially square, large, thin film island at five times for $\theta_s = 5\pi/6$: (a) $t = 0$; (b) $t = 15.63$; (c) $t = 31.25$; (d) $t = 125.00$; and (e) $t = 312.50$. The right column figures show the cross-section profile of the island along the x- or diagonal direction across the origin.

that this pinch-off to form two separate islands (for the island of initial aspect ratio of 140) is consistent with the number of pinch-off events prediction for these conditions by Dornel et al. [13].

5.4. Three-dimensional simulations

As described above, the phase field simulation method proposed is just as easily applied in 3D as it was in 2D.

In this section, we report the results of three interesting applications of the temporal evolution of initially rectangular and square thin film islands on a substrate. Fig. 12 shows the evolution of a rectangular thin film island, initially located in the three-dimensional region $[-0.8,0.8]\times[-0.1,0.1]\times[0,0.1]$ (i.e. $L_x=1.6$, $L_y=0.2$ and $L_z=0.1$). The computational parameters were $\Omega=[-1,1]\times[-0.5,0.5]\times[0,0.5]$, $\varepsilon=0.005$ and $\Delta t=1/1280$. As shown in Fig. 12b, the long, thin island quickly adjusts its numerical contact angle to the prescribed value $\theta_s=5\pi/6$, the ends round, become bulbous (Fig. 12b) and retract (Fig. 12c). The center of the island thins (Fig. 12c), hits the substrate and pinches off in a Rayleigh instability-like form, eventually forming a pair of islands (Fig. 12d) that equilibrate into truncated spherical shapes (Fig. 12e).

Figs. 13 and 14 show the evolution of two, initially square, thin film islands of different sizes for the case of a $\theta_s=5\pi/6$ wetting angle. In these figures, the island shapes were initially small $L_x=L_y=1.6$, $L_z=0.05$ (Fig. 13) and large $L_x=L_y=3.2$, $L_z=0.05$ (Fig. 14). In both cases, the contact angles are rapidly established all around the island perimeter and the initially straight island edges begin to retract, with the corners retracting more slowly than other parts of the edge (see Figs. 13b and 14b). In the small island case, the corners become bulbous (Fig. 13b) and the island center thins as the edges retract (Fig. 13c). Eventually, the corners catch up with the edges, and the island center starts to thicken as the island shape approaches its equilibrium truncated sphere shape (Fig. 13d and e). In the large island case (Fig. 14), the edges form several ripples as they retract (Fig. 14b and c) and the island center thins (Fig. 14d). At a late time, the center of the island surface center comes into contact with the substrate and forms a large hole (Fig. 14e). The island continues to evolve, breaking into four isolated islands via several Rayleigh instabilities (not shown). The above numerical results are consistent with the evolution of square islands observed in the experiments of Ye and Thompson [2].

6. Conclusions

We have proposed a novel phase field approach for simulating the solid-state dewetting of thin films and the evolution of thin film islands on a substrate. The evolution is governed by the Cahn–Hilliard equation with isotropic surface tension and variable scalar mobility. Our approach easily handles the complex boundary conditions arising from the features of the solid-state dewetting problem. Compared with traditional front-tracking methods, this approach does not explicitly track the moving surface but can naturally capture the topological changes that occur during the evolution of the film/island morphology. The numerical method is based on a highly efficient, stabilized, semi-implicit numerical algorithm, which makes full use of discrete cosine and sine transforms. The extension of the model and numerical algorithms from 2D to 3D is straightforward. We performed a series of numerical experiments to demonstrate that the algorithm has excellent numerical stability and that the long-time numerical solutions converge to the theoretical equilibrium state in the limit of small interface width parameter ε. Numerical results are presented in two- and three-dimensional simulations that capture many of the complexities associated with solid-state dewetting experiments [1,2].

While, in the present model, we have focused on the case of isotropic surface energy and diffusion, the model is generalizable to the anisotropic case. Such anisotropy has recently been shown to be important in the retraction of patterned holes in thin films and patterned islands on substrates [3,4]. Future extensions also include a full asymptotic analysis of the relation between the sharp interface and phase field model, and the development of an adaptive mesh strategy to reduce the computational cost associated with the currently employed regular meshing.

Acknowledgements

This work was supported by the Academic Research Fund of Ministry of Education of Singapore Grant R-146-000-120-112 (W.J. and W.B.). C.V.T. thanks the Singapore-MIT Alliance for support of this work. We thank Professor Jie Shen for stimulating discussions on the numerical discretization. Part of the work was done when the second author was visiting Beijing Computational Science Research Center in 2012.

References

[1] Ye J, Thompson CV. Appl Phys Lett 2010;97:071904.
[2] Ye J, Thompson CV. Phys Rev B 2010;82:193408.
[3] Ye J, Thompson CV. Acta Mater 2011;59:582.
[4] Ye J, Thompson CV. Adv Mater 2011;23:1567.
[5] Mordehai D, Kazakevich M, Srolovitz DJ, Rabkin E. Acta Mater 2011;59:2309.
[6] Jiran E, Thompson CV. J Electron Mater 1990;19:1153.
[7] Jiran E, Thompson CV. Thin Solid Films 1992;208:23.
[8] Srolovitz DJ, Safran SA. J Appl Phys 1986;60:247.
[9] Srolovitz DJ, Safran SA. J Appl Phys 1986;60:255.
[10] McCallum MS, Voorhees PW, Miksis MJ, Davis SH, Wong H. J Appl Phys 1996;79:7604.
[11] Wong H, Voorhees PW, Miksis MJ, Davis SH. Acta Mater 2000;48:1719.
[12] Du P, Khenner M, Wong H. J Comput Phys 2010;229:813.
[13] Dornel E, Barbe JC, Crecy F, Lacolle G, Eymery J. Phys Rev B 2006;73:115427.
[14] Chen LQ. Annu Rev Mater Res 2002;32:113.
[15] Folch R, Casademunt J, Machado AH, Piscina LR. Phys Rev E 1999;60:1734.
[16] Karma A, Kessler DA, Levine H. Phys Rev Lett 2001;87:045501.
[17] Zhang L, Chen LQ, Du Q. Acta Mater 2008;56:3568.
[18] Wang YU, Jin YM, Cuitino AM, Khachaturyan AG. Acta Mater 2001;49:1847.
[19] Mullins WW. J Appl Phys 1957;28:333.
[20] Young T. Philos Trans R Soc Lond 1805;95:65.
[21] Chopp DL, Sethian JA. Inter Free Bound 1999;1:1.
[22] Sethian JA. Commun Math Phys 1985;101:487.
[23] Braids A. Oxford lecture series in mathematics and its applications 22. Γ-convergence for beginners. New York: Oxford University Press; 2002.
[24] Modica L, Mortola S. Boll Un Mat Ital A 1977;14(5):526.

[25] Jacqmin D. J Fluid Mech 2000;402:57.
[26] Yue P, Zhou C, Feng J. J Fluid Mech 2010;645:279.
[27] Cahn JW, Hilliard JE. J Chem Phys 1958;28:258.
[28] Gugenberger C, Spatschek R, Kassner K. Phys Rev E 2008;78:016703.
[29] Cahn JW, Elliott CM, Novick-Cohen A. Euro J Appl Math 1996;7:287.
[30] Elliott CM, Garcke H. SIAM J Math Anal 1996;27:404.
[31] Zhu JZ, Chen LQ, Shen J, Tikare V. Phys Rev E 1999;60:3564.
[32] Shen J, Yang XF. SIAM J Sci Comput 2010;32:1159.
[33] He YN, Liu YX, Tang T. Appl Numer Math 2007;57:616.
[34] Press WH, Teukolsky SA, Vetterling WT, Flannery BP. Numerical recipes: the art of scientific computing. 3rd ed. Cambridge: Cambridge University Press; 2007.
[35] FFTW Homepage Website. <http://www.fftw.org>.
[36] Lee HG, Kim J. Comput Fluids 2011;44:178.